TRANSACTIONS

OF THE INSTITUTE OF

FLUID-FLOW MACHINERY

PRACE

INSTYTUTU MASZYN PRZEPŁYWOWYCH

106

ROMUALD RZĄDKOWSKI[1] and VITALLY GNESIN[2]

The numerical and experimental verification of the 3D inviscid flutter code

In this study the numerical calculations were performed to compare the theoretical results of 3D inviscid flutter code with experimental results due to Bölcs and Fransson. The calculations were carried out for the torsional oscillations of the compressor cascade known as the First Standard Configuration, and the bending oscillations of the steam turbine cascade which has become the Fourth Standard Configuration. The developed numerical algorithm solves the Euler equation in conservative form, which is integrated by using the explicit monotonous second-order accurate Godunov-Kolgan finite-volume scheme and the moving hybrid grid. The structural model is based on the 3D and 1D models. The comparison of calculated and experimental results for the 1st and 4th Standard Configurations has shown the good quantitative and qualitative agreement for both integral performances (aerodamping coefficient) and local performances (unsteady pressure amplitude and phase distribution).

1. Introduction

Aeroelasticity phenomena are characterised by the interaction of fluid and structural domains, and are described by equations which are non-linear in the general case. In turbomachinery environments, the problem is further compounded by the fact that blades vibrate with a relative phase with respect to each other, the value of which is not necessarily known. Most prediction methods tend to treat the two domains separately and they usually assume some critical interblade phase angle for which the flutter analysis is carried out for a single passage. More recent approaches, the so-called integrated or coupled methods, link the structural and fluid domains via a set of boundary conditions that must be satisfied simultaneously throughout the solution phase. Multi-stage, multi-passage models, including whole annulus representations, are also starting to emerge as computing power becomes more readily available. A literature review is beyond the scope of this paper but a survey of aeroelasticity methods with emphasis on

---

[1]Institute of Fluid Flow Machinery, Department of Dynamics of Machines, Fiszera 14, 80-952 Gdańsk, Poland

[2]Ukrainian National Academy of Sciences, 2/10 Pozharsky St., Kharkov 3, 10046 Ukraine

turbomachinery applications can be found in Marshall and Imregun [1].

In this study the numerical calculations were performed to compare the theoretical results of 3D inviscid flutter code with experiments presented by Bölcs and Fransson [2]. The calculations were carried out for the torsional oscillations of the compressor cascade known as the First Standard Configuration, and the bending oscillations of steam turbine cascade, which has become the Fourth Standard Configuration. The developed numerical algorithm solves the Euler equation in conservative form. The Euler equations are integrated by using the explicit monotonous second-order accurate Godunov-Kolgan finite-volume scheme and moving hybrid grid [3, 4]. The structural model is based on the 3D and 1D models. The comparison of calculated and experimental results for the 1st and 4th Standard Configurations has shown the good quantitative and qualitative agreement for both integral performances (aerodamping coefficient) and local performances (unsteady pressure amplitude and phase distribution).

2. The numerical verification of the flutter code

On the base of mathematical model [3, 4] the algorithm and numerical code were developed.

Validation of the computational results for unsteady flows through the oscillating blade row becomes more difficult, because experimental data for three-dimensional flows are currently hardly available in the published literature. Therefore comparisons between numerical and experimental results for a simple cascade geometry at inviscid flow conditions was done.

In this study the numerical calculations were performed to compare the theoretical results with experiments presented by Bölcs and Fransson [2]. The calculations were carried out for the torsional oscillations of the compressor cascade known as the First Standard Configuration, and the bending oscillations of steam turbine cascade, which has become the Fourth Standard Configuration.

Both cascades were experimentally investigated in the nonrotating annular cascade tunnel at the Swiss Federal Institute of Technology, Lausanne, where the first cascade was run in low subsonic flow, while the second cascade was investigated in transonic flow. Air was used as working medium.

Numerical investigations were performed with use H-H or H-O grids, including $10 \times 30 \times 60$ cells in radial, circumferential and axial directions respectively.

2.1. Torsional oscillations of compressor cascade (1st Standard Configuration)

The cascade configuration being investigated, consists of eleven vibrating compressor blades, geometrical characteristic of which together with oscillation regimes are presented in Fig. 1 and in Tab. 1.
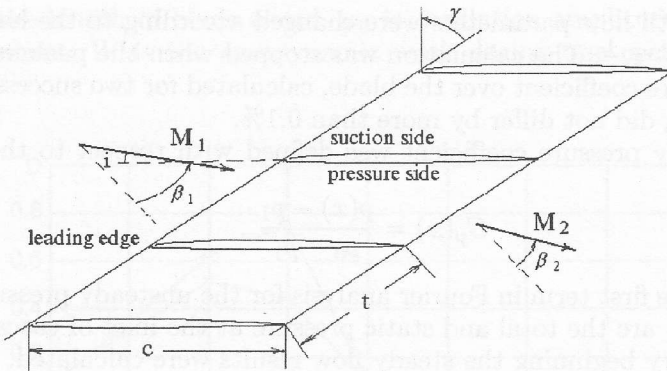
Fig. 1. 1st Standard Configuration.

Table 1. Geometry and operating data of cascade STC1

blade length	L	0.254 m
chord length	c	0.1524 m
circular are camber		10°
thickness-to-chord ratio		0.06
stagger angle	γ	55°
pitch-to-chord ratio	t/c	0.75
inflow angle	β_1	36°
incidence angle		-6°
inlet Mach number	M_1	0.18
outflow angle	β_2	28°
outflow Mach number	M_2	0.15
vibration frequency	ν	20 Hz
reduced frequency	$k = (c \cdot 2\pi\nu)/v_2$	0.121
vibration amplitude	φ_0	$2^{\circ}(0.0349$ deg$)$
interblade phase angle	δ	$0^{\circ}, \pm45^{\circ}, \pm90^{\circ}, 180^{\circ}$

All blades perform the torsional harmonic oscillations by the same law and constant interblade phase angle (IBPA). The positive direction of IBPA has been chosen in the direction opposite to the direction of rotation.

For the time-dependent numerical results $C(t)$ the Fourier analysis was used:

$$C(t) = C_0 + \sum_{n=1}^{\infty} (C_n^a \cos n2\pi\nu t + C_n^b \sin n2\pi\nu t), \qquad (1)$$

where C_0, C_n^a, C_n^b are Fourier coefficients; ν – oscillation frequency.

Aerodynamic calculations were continued till the steady state results have

been achieved. All flow parameters were changed according to the harmonic law with period of $T = \frac{1}{\nu}$. The calculation was stopped when the peak values of the unsteady pressure coefficient over the blade, calculated for two successive periods of blade motion, did not differ by more than 0.1%.

The unsteady pressure coefficient was defined with respect to the inlet flow values:

$$\overline{C}_p(x) = \frac{p(x) - p_1}{p_0 - p_1}, \tag{2}$$

where $p(x)$ is the first term in Fourier analysis for the unsteady pressure over the blade; p_0 and p_1 are the total and static pressure at the inlet of cascade.

From the very beginning the steady flow results were calculated. The steady flow parameters are the starting point for unsteady flow calculations.

The comparison between the theoretical and experimental steady state pressure coefficient distribution along the chord is shown in Fig. 2. Solid lines are the numerical results. The integers 1 and 2 correspond to the suction and pressure sides respectively. The agreement between the experimental and numerical results is good. Only small deviations are observed near the leading edge on the pressure side. It can be explained by the difference in measurement of the incidence angle in the experiment and the assumed incident angle in numerical calculations (this difference is about 2.5°).
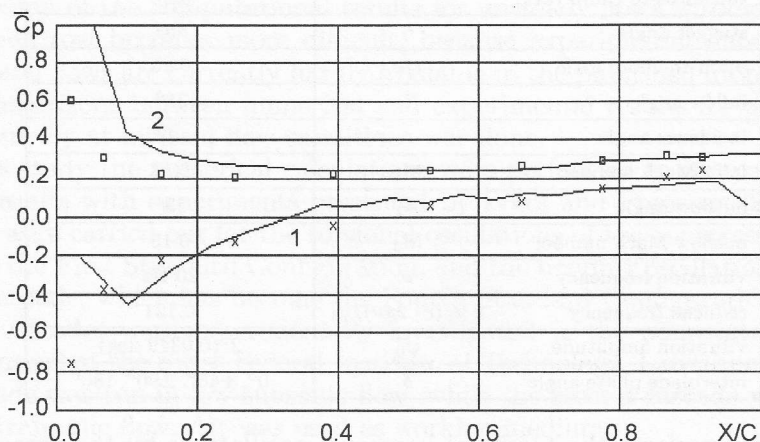

Fig. 2. Time averaged blade surface pressure coefficient. Theory: ——— ; experiment: □ □ – pressure side, × × – suction side.

The aeroelastic behaviour of the palisade without taking into account the mechanical damping is defined by the aerodamping coefficient D:

$$D = -\frac{W}{(p_0 - p_1)\pi c^3 \varphi_0^2}, \quad W = \int_0^{\frac{1}{\nu}} M \frac{d\varphi}{dt} dt, \tag{3}$$

where c is the length of blade chord, φ_0 is oscillation amplitude, M is aerodynamical moment, W is the aerodynamic work during one cycle of oscillation.
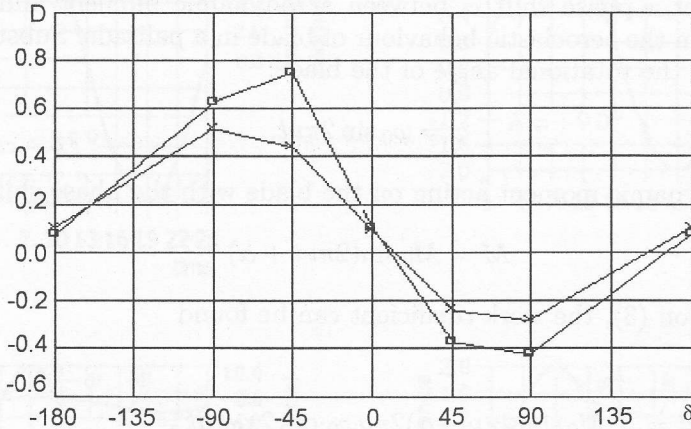

Fig. 3. Aerodamping coefficient in dependence of IBPA □ – experimental results, × – numerical results.

Fig. 3 shows the aerodamping coefficient as a function of the interblade phase angle δ. Positive values of the aerodamping coefficient correspond to the dissipation of the blade energy to the flow (aerodamping), the negative values – to the transfer of the energy from the main flow to the blade (self-excitation or flutter). The agreement between numerical ("crosses") and measured ("small squares") results is satisfactory, although the absolute values of calculated aerodamping coefficient in the vicinity of its maximal values ($\delta = \pm 90^o$) are lower then for the corresponding experimental data.

It should be pointed out that the aerodamping coefficient dependence on IBPA has a typical sinusoidal form. Moreover, for IBPA close to zero ($\delta = 0^o$) the aerodamping is positive. It confirms the known theoretical fact about the impossibility of beginning of the pure torsional flutter for the single wing. It is seen from Fig. 3 that the amplitude of torsional blades oscillations with IBPA from -180 to 20 deg, are decreasing (damping), whereas for IBPA from 20 to 140 deg the amplitude of oscillation is increasing (flutter condition, the aerodamping coefficient less than zero).

The cascade flutter is dependent on the phase lag of the aerodynamic load with respect to the blade motion, which in turn depends on the interblade phase angle of blades oscillations.

The torsional displacement of the blade φ (with respect to the mean blade position) and the values of the aerodynamic moments M acting on the blade, during one cycle of oscillations and for IBPA $\delta = 0^o = 0,\ 180^o;\ \pm 45^o;\ \pm 90^o$ was shown in Fig. 4. The aerodynamic moment is the harmonic function. For IBPA

equal to $\delta = 0^o$; -45°; -90° there is a phase shift of moment relatively to the blade motion in the direction of lag time, but for IBPA of $\delta = +45^o$; $+90^o$ the aerodynamic moment proceeds the blade motion.

Let us obtain the analytical expression for the work coefficient W to proof the influence of a phase shift α between aerodynamic moment and the blade displacement on the aeroelastic behaviour of blade in a palisade. Substituting the expressions for the rotational angle of the blade:

$$\varphi = \varphi_0 \sin 2\pi\nu t,$$

and the aerodynamic moment acting on the blade with the phase shift α:

$$M = M_0 \sin(2\pi\nu t + \alpha)$$

into the equation (3), the work coefficient can be found

$$W = \int\limits_0^{\frac{1}{\nu}} M \frac{d\varphi}{dt} dt = \int\limits_0^{\frac{1}{\nu}} M_0 \sin(2\pi\nu t + \alpha) 2\pi\nu\varphi_0 \cdot \cos 2\pi\nu t \, dt =$$

$$= \int\limits_0^{\frac{1}{\nu}} 2\pi\nu M_0\varphi_0 (\sin 2\pi\nu t \cdot \cos 2\pi\nu t \cos \alpha + \cos 2\pi\nu t \cdot \cos 2\pi\nu t \cdot \sin \alpha) dt =$$

$$= 2\pi\nu M_0\varphi_0 \int\limits_0^{\frac{1}{\nu}} \left(\frac{1}{2} \sin 4\pi\nu t \cdot \cos \alpha + \cos^2 2\pi\nu t \cdot \sin \alpha \right) dt =$$

$$= 2\pi\nu M_0\varphi_0 \int\limits_0^{\frac{1}{\nu}} \left(\frac{1}{2} \sin 4\pi\nu t \cdot \cos \alpha + \frac{1}{2} \sin \alpha + \frac{1}{2} \cos 4\pi\nu t \cdot \sin \alpha \right) dt =$$

$$= 2\pi\nu M_0\varphi_0 \left[\cos \alpha \cdot \frac{1}{8} \cos 4\pi\nu t + \frac{1}{2} \sin \alpha t + \sin \alpha \cdot \frac{1}{8} \sin 4\pi\nu t \right]\Big|_0^{\frac{1}{\nu}} t =$$

$$= 2\pi\nu M_0\varphi_0 \cdot \frac{1}{2} \sin \alpha \cdot \frac{1}{\nu} = \pi M_0\varphi_0 \sin \alpha$$

Thus,
$$D = -W = -\pi M_0\varphi_0 \sin \alpha \tag{4}$$

where M_0 and φ_0 are the amplitudes of both aerodynamic moment and blade oscillations respectively; α is the lead angle (or the lag angle, if $\alpha < 0$) of the moment with respect to the blade motion. The sign of the angle α (see Eq. 4) determines the sign of the aerodynamic work W, i.e. when $\alpha > 0$ $(W > 0; D < 0)$ the flow energy transfer to the blade (self-excitation), when $\alpha < 0$ $(W < 0; D > 0)$
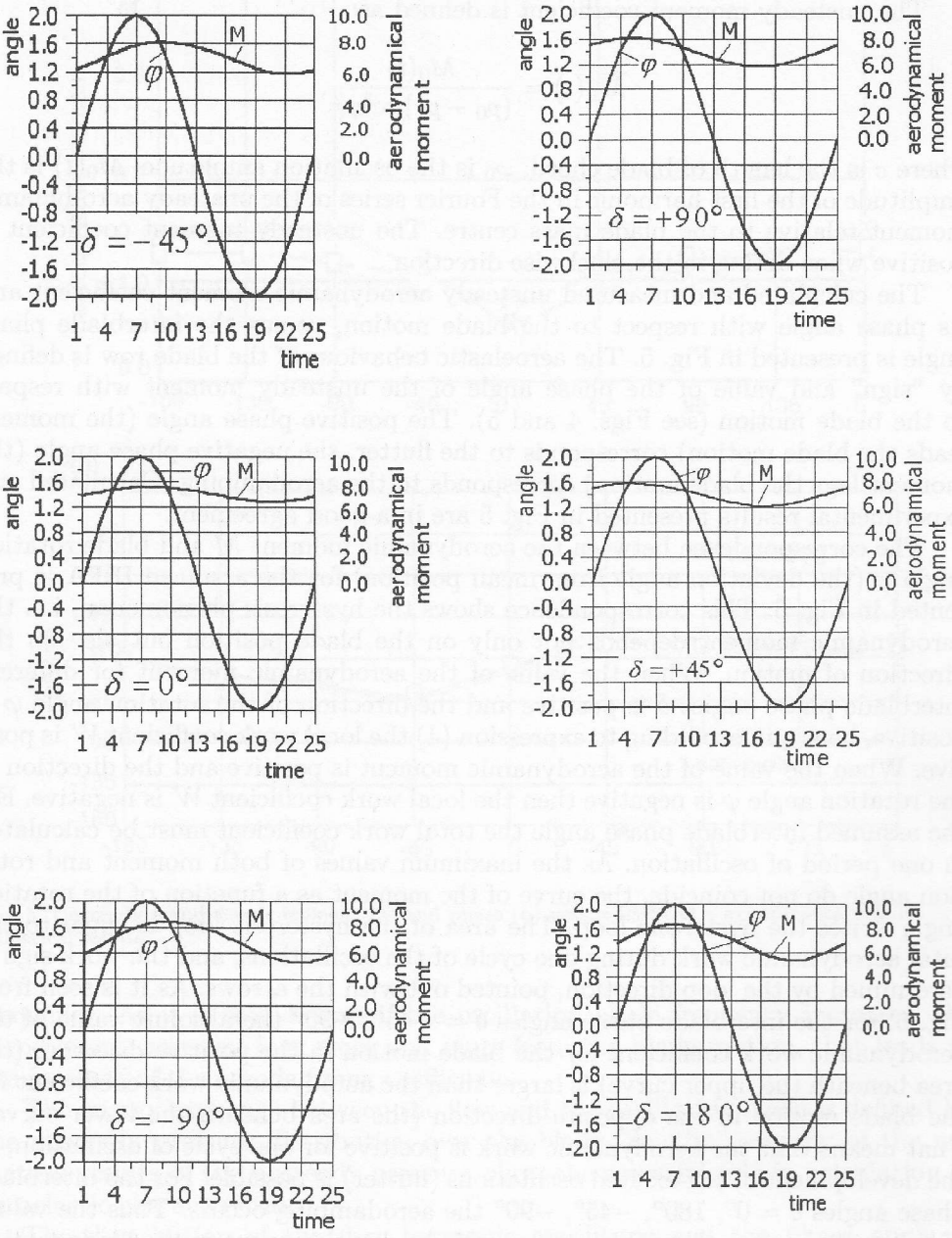
Fig. 4. The aerodynamic moment and the blade rotation angle during one cycle of oscillations.

the energy of oscillating blade dissipates to the main flow (aerodamping).

The unsteady moment coefficient is defined as:

$$\overline{M}_0(t) = \frac{M_0(t)}{(p_0 - p_1)\pi c^3 \varphi_0^2},$$

where c is the length of blade chord; φ_0 is the oscillation amplitude; $M_0(t)$ is the amplitude of the first harmonic in the Fourier series of the unsteady aerodynamic moment relative to the blade mass centre. The unsteady moment coefficient is positive when acting in the clockwise direction.

The calculated and measured unsteady aerodynamic moment coefficient and its phase angle with respect to the blade motion, versus the interblade phase angle is presented in Fig. 5. The aeroelastic behaviour of the blade row is defined by "sign" and value of the phase angle of the unsteady moment with respect to the blade motion (see Figs. 4 and 5). The positive phase angle (the moment leads the blade motion) corresponds to the flutter, the negative phase angle (the moment lags the blade motion) corresponds to the aerodamping. Calculated and experimental results presented in Fig. 5 are in a good agreement.

The correspondence between the aerodynamic moment M and blade rotation angle φ (the deviation angle from mean position) for the assumed IBPA is presented in Fig. 6. This correspondence shows the hysteresis phenomenon, i.e. the aerodynamic moment depends not only on the blade position but also on the direction of motion. When the value of the aerodynamic moment for different interblade phase angles δ is positive and the direction of the rotation angle φ is positive, hence, in according to expression (4) the local work coefficient W is positive. When the value of the aerodynamic moment is positive and the direction of the rotation angle φ is negative then the local work coefficient W is negative. For the assumed interblade phase angle the total work coefficient must be calculated in one period of oscillation. As the maximum values of both moment and rotation angle do not coincide, the curve of the moment as a function of the rotation angle writes the hysteresis loop. The area of the hysteresis loop is equal to the total aerodynamic work during one cycle of the oscillations, and the work sign is determined by the loop direction, pointed out with the arrows. As it is seen from Fig. 6, for the interblade phase angles $\delta = +45^o$, $+90^o$ the absolute value of the aerodynamic work coefficient for the blade motion in the positive direction (the area beneath the upper curve) is larger than the aerodynamic work coefficient for the blade motion in the opposite direction (the area beneath the lower curve). That means that the aerodynamic work is positive for one cycle of oscillation, so the development of self-excited oscillations (flutter) is possible. For the interblade phase angles $\delta = 0^o$, 180°, -45°, -90° the aerodamping occurs. Thus the values of the shift phase angle of the aerodynamic load with respect to the blade motion (which in turn is caused by the interblade phase angle), allows to understand the physical mechanism of the cascade flutter origin.

It should be pointed out that the phase angle of the aerodynamic load with respect to the blade motion depends not only on IBPA, but on the oscillation
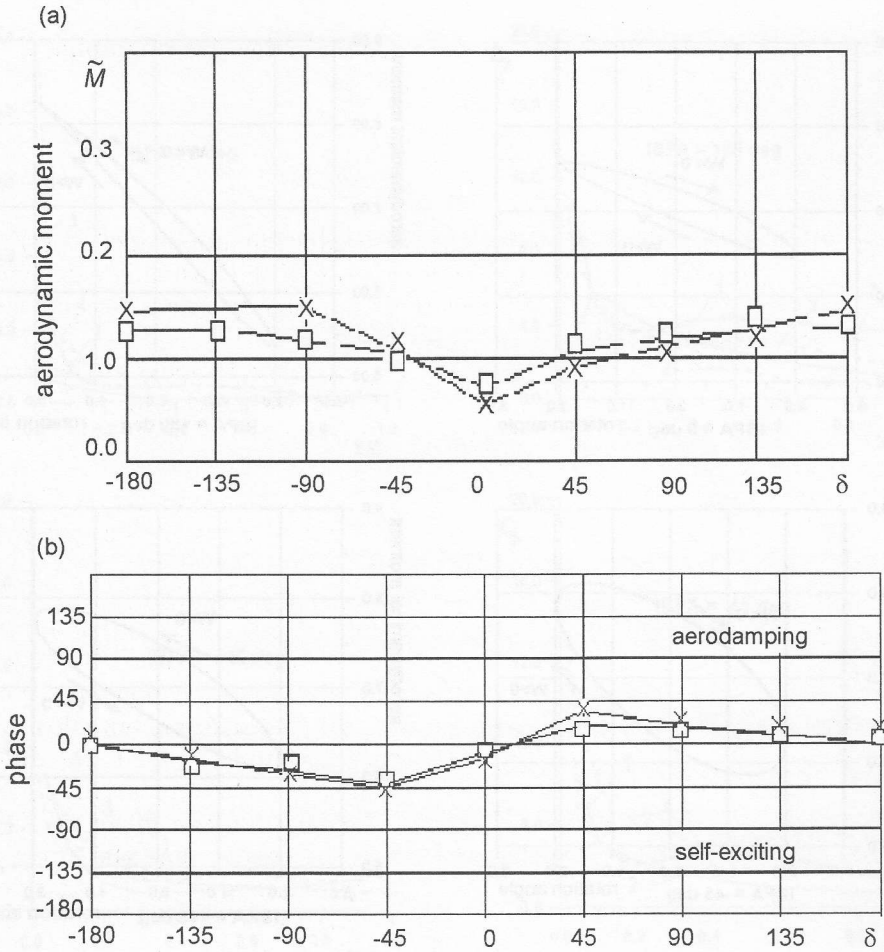
(a)

(b)

Fig. 5. Unsteady aerodynamic moment (a) and phase (b) versus IBPA □ – experimental results, × – numerical results.

frequency. As it is seen below, if the oscillation blade frequency increases, the aerodynamic moment lags more and more from the blade motion, that leads to the increase of the aerodamping coefficient.

The energy exchange between the flow and the oscillating blade is defined by the unsteady pressure distribution over the blade. So, the accuracy of the numerical results of the unsteady pressure plays the essential role in calculation of aeroelastic characteristics.

The distribution of the first harmonic amplitude and the phase angle of the unsteady pressure coefficient along the blade chord for different IBPA and $M = 0.16$ were shown in Figs. 7 and 8.

The agreement between theoretical (solid lines) and experimental results (dashed line) is quite good.

R. Rządkowski and V. Gnesin
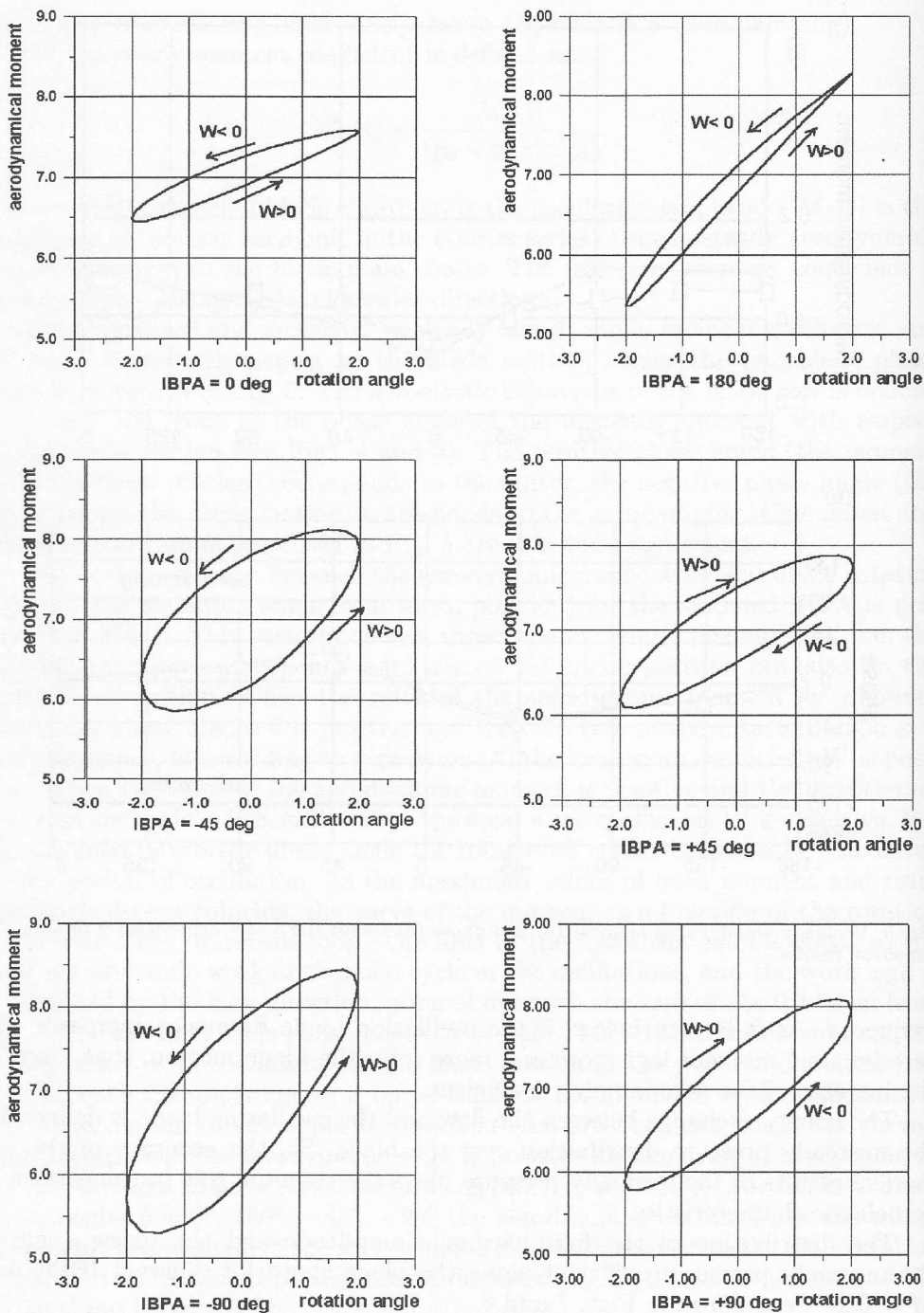
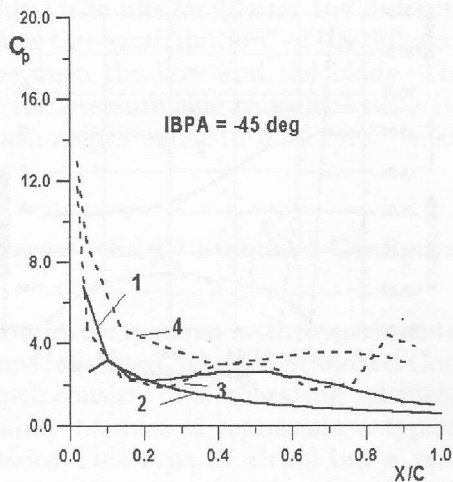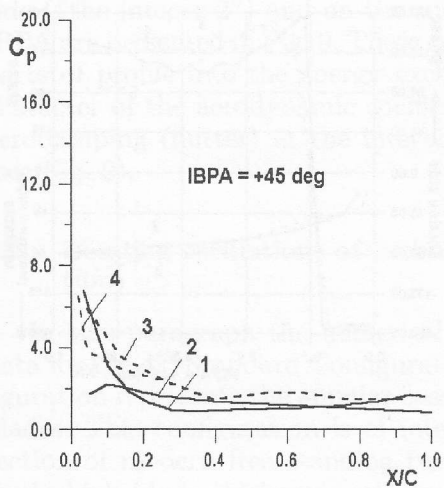Fig. 6. Aerodynamical moment in dependence on blade rotation angle (hysteresis loop).
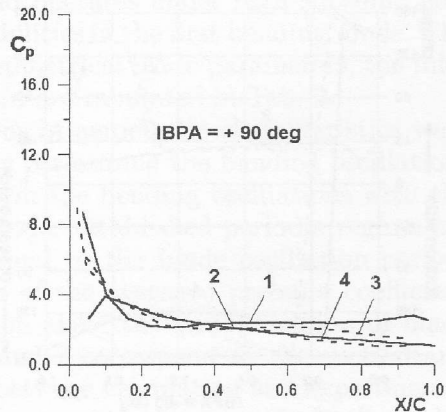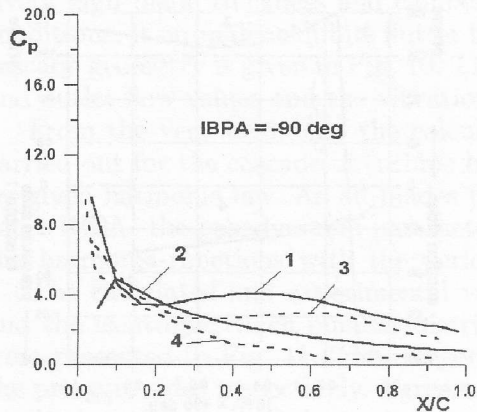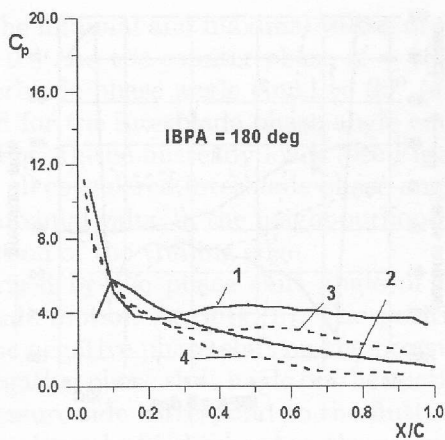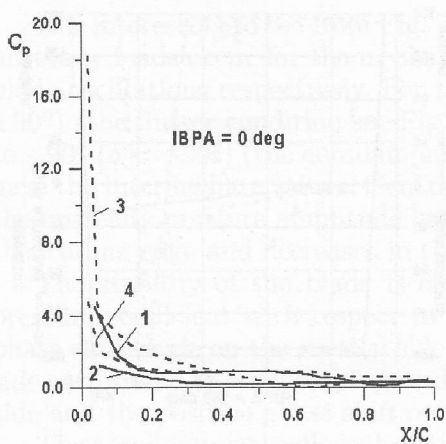
Fig. 7. The unsteady pressure amplitude distribution over the blade chord; suction side: 1 – numerical, 3 – experimental; and pressure side: 2 – numerical, 4 – experimental.
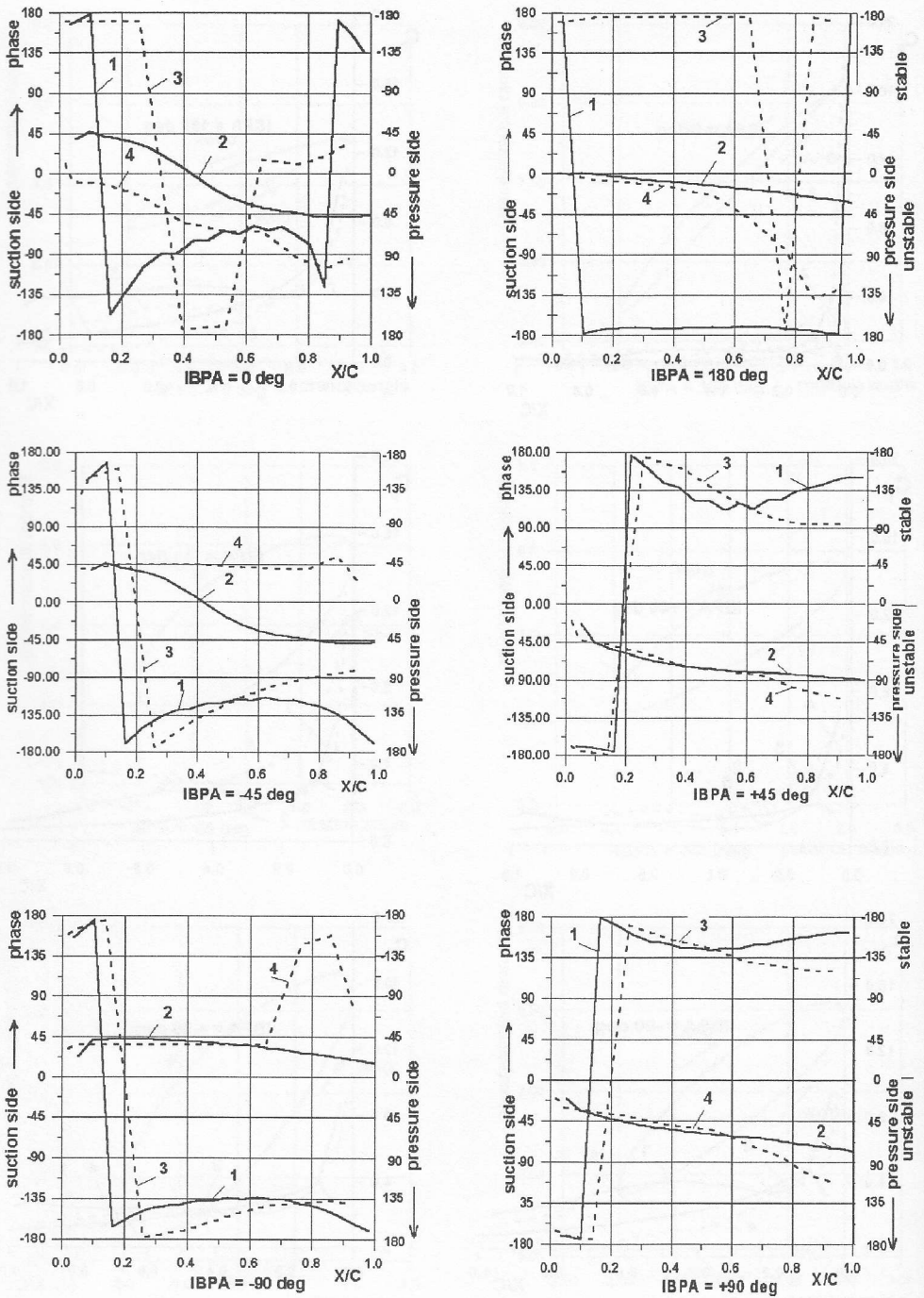
Fig. 8. The unsteady pressure amplitude distribution over the blade chord; suction side: 1 – numerical, 3 – experimental; and pressure side: 2 – numerical, 4 – experimental.

It is interesting to see from Fig. 7 that the minimal and maximal values of the unsteady loads occur for the in phase ($\delta = 0^o$) and the counter phase ($\delta = 180^o$) blade oscillations respectively. For the interblade phase angle equal to 90° ($\delta = \pm 90^o$) (the flutter condition see Fig. 3) and for the interblade phase angle equal to -90° ($\delta = -90^o$) (the aerodamping, see Fig. 3); the unsteady loads (see Fig. 7) have the intermediate values. Generally for all considered interblade phase angles the unsteady pressure amplitude has the maximal value in the neighbourhood of the leading edge and decreases in the direction of the trailing edge.

The stability of the blade is characterised by the phase shift angle of the pressure coefficient with respect to the blade motion (see Fig. 8). The positive phase shift angle on the suction side and the negative phase shift on the pressure side correspond to aerodamping, and the negative phase shift angle on the suction side and the positive phase shift on the pressure side correspond to the flutter.

The aerodamping coefficient distribution along the blade chord on the pressure side ("the integer 2") and on the suction side ("the integer 1") for the different IBPA are presented in Fig. 9. These curves show the "contribution" of the different parts of profile into the energy exchange between the flow and the blade. The character of the aerodynamic coefficient on the pressure side cause the negative aerodamping (flutter) at the interblade phase angles equal to $\delta = \pm 45^o, +90^o$ (see Fig. 9).

2.2.   Bending oscillations of turbine blade row (the 4th Standard Configuration)

In this paragraph the numerical results and comparison with experimental data for the 4th Standard Configuration [2] are presented. The 4th Standard Configuration represents the annular cascade which consists of 20 vibrating prismatic blades. This configuration is of interest mainly because it represents a typical section of modern free standing turbine blades This type of airfoil has a relatively high blade thickness and camber, and operates under high subsonic flow conditions. It normally exhibits flutter instabilities in the first bending mode. The cascade geometry is given in Fig. 10. The geometrical blade parameters, the inlet and outlet flow values and the vibration data are tabulated in Tab. 2.

From the very beginning the calculations of aeroelastic characteristics were carried out for the cascade of turbine blades performing the bending oscillations by given harmonic law. As all blades perform the bending oscillations with the same IBPA, the gasodynamic parameters under established periodic regime are the harmonic functions with the period equal to the blade oscillation period.

The calculated and experimental values of the averaged pressure coefficient and the isentropic Mach number distribution along the middle section of blade were presented in Fig. 11. The integers 1 and 2 correspond to the suction and the pressure sides respectively. Agreement between calculation and experimental results is satisfactory. Only small discrepancy is noticeable near the leading edge at approximately 30 percent of the chord length on the suction side.

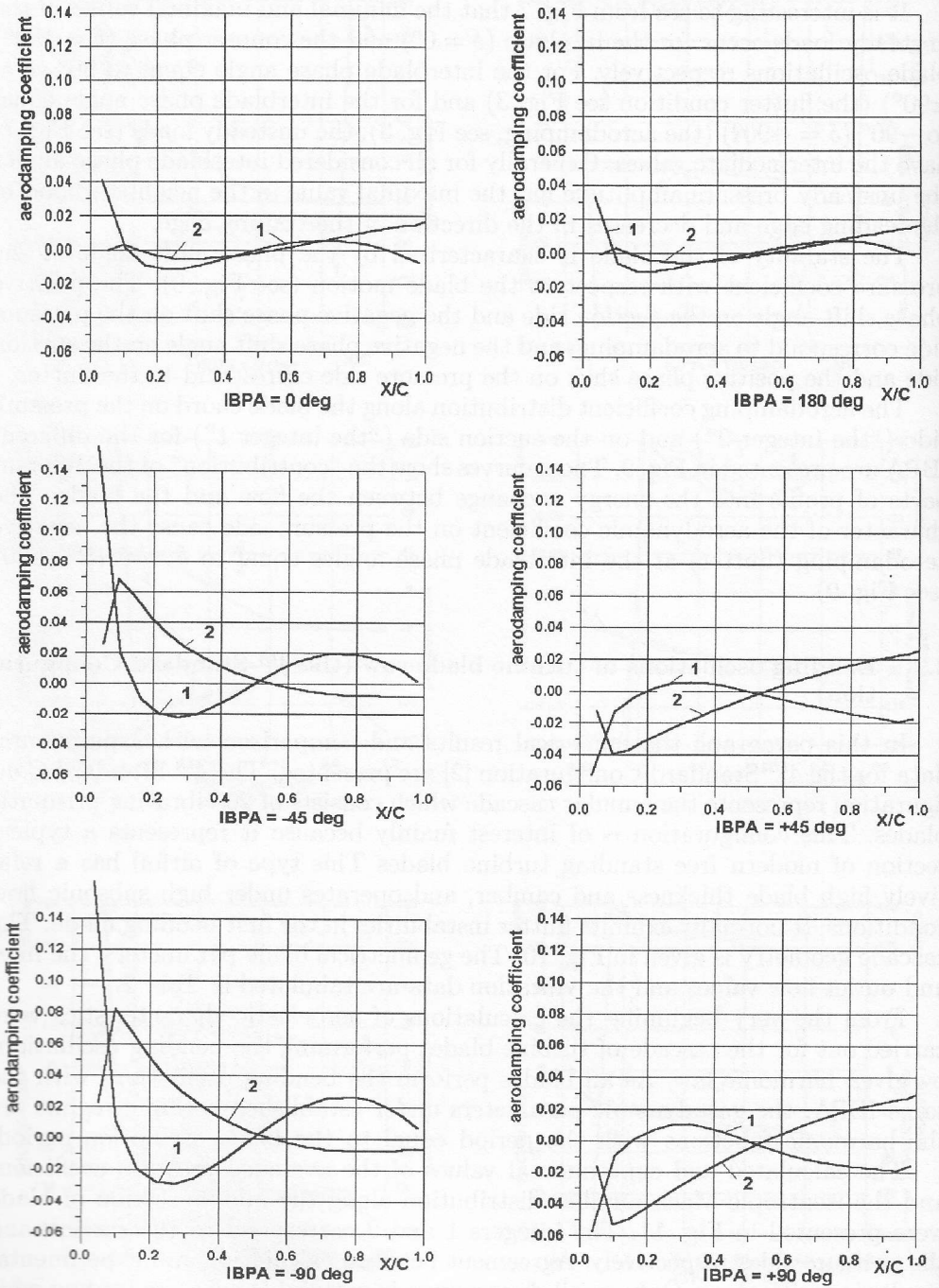The influence of IBPA on the aerodamping coefficient for an assumed ben-

Fig. 9. The aerodamping coefficient distribution over the blade chord 1 – suction side; 2 – pressure side.

ding oscillations was shown in Fig. 12. The aerodamping coefficient D calculated during one cycle of oscillations is defined for the bending motion as:

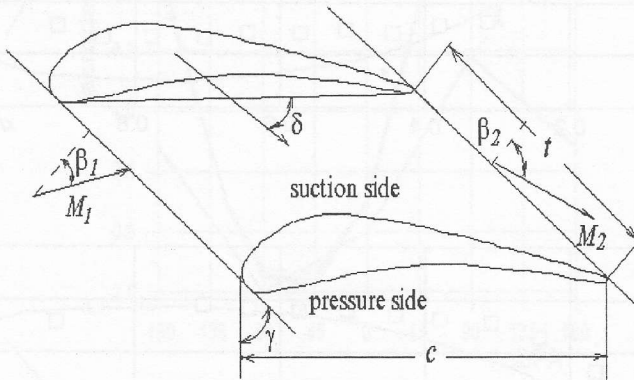$$D = -\frac{W}{(p_0 - p_1)\pi c h_0^2}; \qquad W = \int_0^{\frac{1}{\nu}} -\mathbf{F} \cdot \mathbf{v}\, dt, \tag{6}$$

Fig. 10. 4th Standard Configuration.

Table 2. Geometry and operating data of cascade STC4

blade length	L	0.04 m
chord length	c	0.0744 m
stagger angle	γ	56.6^o
pitch-to-chord ratio	t/c	0.67 (hub) 0.76 (mid) 0.84 (casing)
inflow angle	β_1	-45°
inlet Mach number	M_1	0.28
outflow angle	β_2	-72°
outflow Mach number	M_2	0.9
bending angle (against chord)		60.4^o
vibratration amplitude	φ_0, h/c	0.0033
vibration frequency	ν	150 Hz
reduced frequency	$k = (c \cdot 2\pi\nu)/v_2$	0.11
interblade phase angle	δ	$0^o, \pm 45^o, \pm 90^o, 180^o$

where h_0 is the amplitude of bending oscillations; $\mathbf{F}$ is the aerodynamic force vector, $\mathbf{v}$ is the blade velocity vector. The sign "minus" in Eq. (6) means that the direction of the force vector is opposite to the positive direction of the blade motion.

The calculated values of aerodamping coefficient in a hub, middle and peripheral sections (denoted with integers 1, 2 and 3 respectively), as well as the
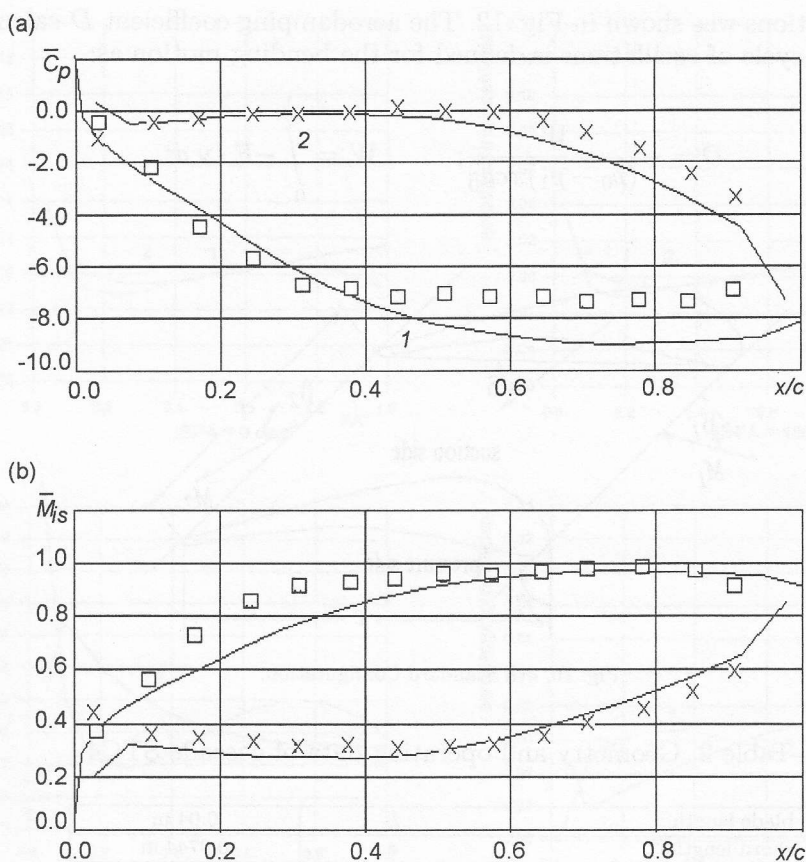
(a)

(b)

Fig. 11. The time averaged pressure coefficient (a) and Mach number (b) distribution over the blade chord. Theory: 1 – suction, 2 – pressure side; experiment: □□ – pressure side, ×× – suction side.

experimental values (curve 4), averaged over the blade length are presented in Fig. 12.

The aerodamping coefficient depends on the interblade phase angle. This dependence has a typical sinusoidal character as for 1st Standard Configuration (see Fig. 3). The values of this coefficient are negative (flutter condition) for the interblade phase angle from -120° to -30° ($-120^o < \delta < -30^o$) and $M = 0.9$. The maximal value of aerodamping occurs at the IBPA equal to 90° ($\delta = +90^o$).

The aerodamping coefficient in this case does not depend on the blade length. The blade is relatively short and prismatic. Experimental values of the aerodamping coefficient (curve 4) coincide qualitatively with calculated results although they differ in the vicinity of maximal aerodamping.

The influence of IBPA on the energy exchange between the flow and the blade
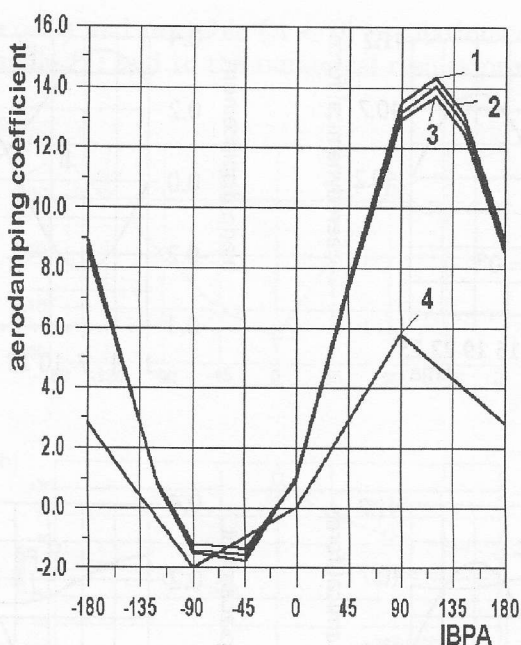
Fig. 12. Aerodamping coefficient in dependence of interblade phase angle. Theory: 1 – casing; 2 – mid; 3 – hub; experiment: 4.

can be expressed analytically by putting the expressions for the blade velocity v:

$$h = h_0 \sin 2\pi\nu t; \quad v = 2\pi\nu h_0 \cos 2\pi\nu t;$$

and the aerodynamic force

$$F = F_0 \sin(2\pi\nu t + \alpha),$$

into the equation (6):

$$W = -\pi F_0 h_0 \sin \alpha. \tag{7}$$

The positive angle α (the force leads the blade moving) corresponds to aerodamping ($W < 0, D > 0$), and on the contrary the negative value of α (the force lags the blade motion) corresponds to self-exciting vibration ($W > 0, D < 0$).

The blade bending displacement h and the aerodynamic force F, acting on the blade, as functions of time, during one cycle of oscillations, for the different values of IBPA were shown in Fig. 13. At the $\delta = -45^o, -90^o$ the aerodynamic force lags the blade motion ($\alpha < 0$), so according to equation (7) the energy is transferred to the blade, (flutter condition, negative aerodamping (see Fig. 12)). If IBPA changes from 0° to 180° and from 45° to 90° the aerodynamic force leads the blade motion ($\alpha > 0$). It corresponds to the positive aerodamping.

The amplitude of the aerodynamic force and the phase angle with respect to the blade motion as functions of interblade phase angles is shown in Fig. 14. The
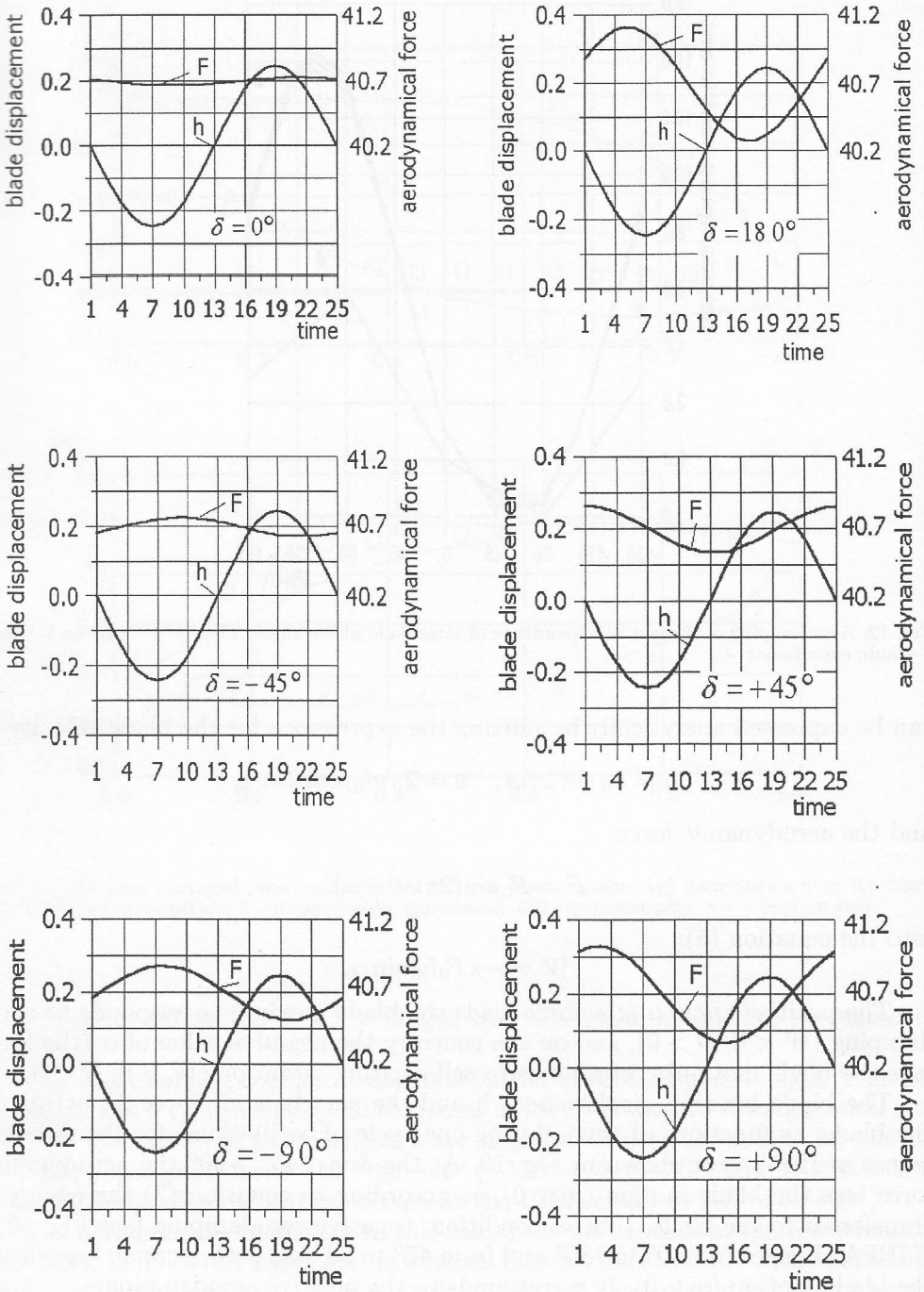
Fig. 13. The aerodynamic load and the blade displacement during one cycle of oscillations.

areas of stable ($\alpha > 0$) and unstable ($\alpha < 0$) oscillations depend on IBPA, and correspond to formula (7) and to the numerical results presented in Fig. 12.
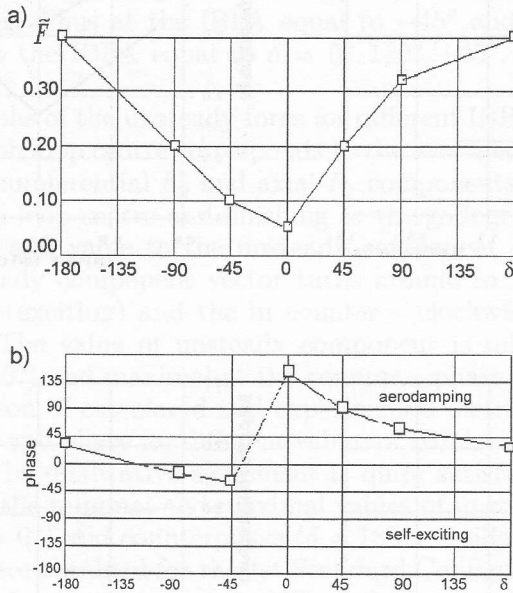

Fig. 14. Unsteady aerodynamic force (a) and phase lead (b) versus IBPA.

Thus the analytical expression (7) and numerical results confirm that at the given law of oscillations the energy exchange and the aeroelastic behaviour of blade row depends on IBPA. The value of transferred or dissipated energy is defined by the phase lead angle (or phase lag angle) of aerodynamical load with respect to the blade motion, as well as by amplitudes of both blade oscillations and unsteady force.

At the given law of oscillations the aerodamping coefficient in considered cascade does not practically depend on the flow regime, for the Mach number in the range from 0.5 to 1.2 ($0.5 \leq M_2 \leq 1.2$) (see Fig. 15). The aerodamping coefficient remains almost constant, and this fact is in a good agreement with the experimental data.

The correspondence between unsteady aerodynamic load and the blade motion for different IBPA values is presented in Fig. 16 (hysteresis loops). Aerodynamical force always is directed from the pressure side to the suction side, i.e. the force vector puts the blunt angle together with the positive direction of y – axis (Fig. 3). So in accordance to the formula (6), the work coefficient is always positive ($D < 0$) when the blade moves in a positive direction h, moreover its value is defined by the area beneath the upper curve with the arrow pointing out the direction of the blade motion. If the blade moves in opposite direction the work coefficient is negative ($D > 0$). The area of hysteresis loop characterises the value
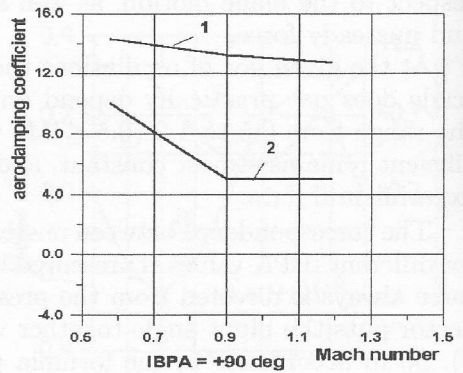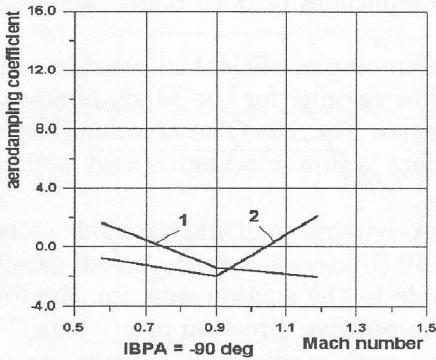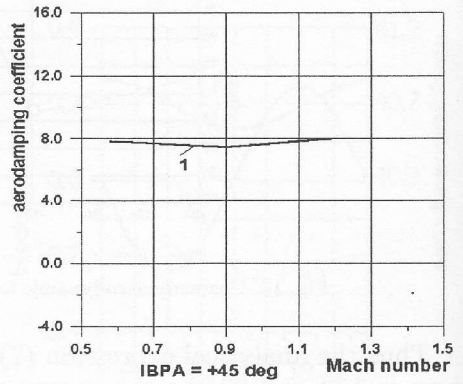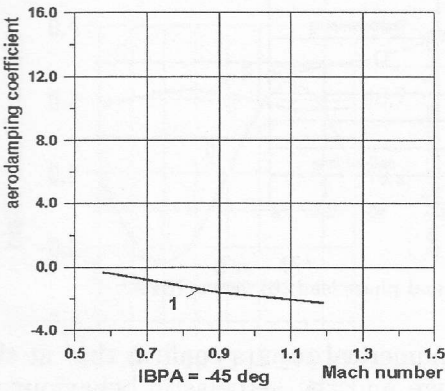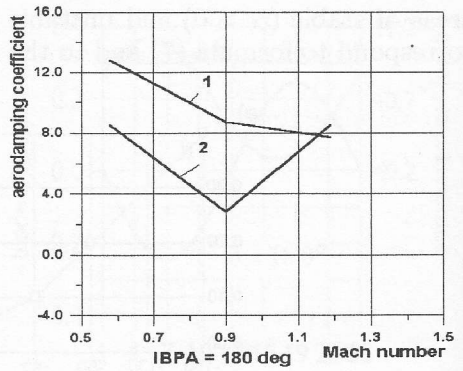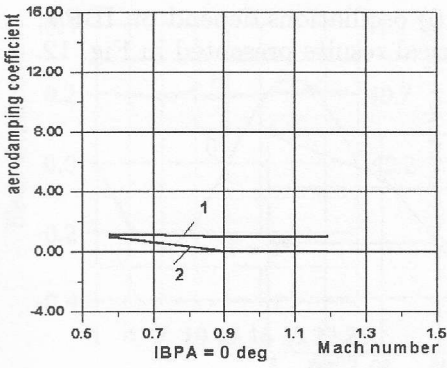
Fig. 15. Aerodamping coefficient in dependence of outlet isentropic Mach number: 1 – theory; 2 – experiment.

of the work coefficient during one cycle of oscillations, and its sign is defined by the loop direction pointed out with the arrow. The clockwise direction of the loop corresponds to positive work (self – exciting), in the counter – clockwise direction – to aerodamping. Thus at the IBPA equal to -45° and 90° ($\delta = -45^o, -90^o$) flutter occurs, at the IBPA equal to $\delta = 0^o, 180^o, +45^o, +90^o$ the aerodamping occurs.

The godographs of the unsteady force for different IBPA are presented in Fig. 17. The godograph loop centre corresponds to the averaged aerodynamic force decomposed on circumferential F_y and axial F_z components. The vector beginning in the godograph loop centre and finishing at the godograph curve, corresponds by the direction and value to the unsteady component of total aerodynamical force. The unsteady component vector turns around in the clockwise direction if $D < 0$, (self – exciting) and the in counter – clockwise direction for $D > 0$ (aerodamping). The value of unsteady component is minimal at the in phase oscillations ($\delta = 0^o$) and maximal at the counter – phase oscillations ($\delta = 180^o$).

The comparison of calculated and experimental distribution of the first harmonic amplitude and phase for different values of IBPA and $M = 0.9$ is presented in Fig. 18, 19. The qualitative agreement is quite satisfactory. As for the compressor cascade, the minimal and maximal values of unsteady pressure occur for the in phase ($\delta = 0^o$) and counterphase ($\delta = 180^o$) oscillations, respectively. The similar results were obtained for the 1st Standard Configuration (see Fig. 7). The maximal values of pressure are up to 20% of the averaged pressure value.

The energy exchange is defined by unsteady pressure phase distribution over the blade (see Fig. 19). The positive pressure phase shift on the pressure side with respect to the blade motion and the negative phase shift on the suction side corresponds to the aerodamping (stability).

The aerodamping coefficient over the blade surface for different IBPA values was shown in Fig. 20. At the IBPA equal to $\delta = -45^o, -90^o$ the negative aerodamping (instability) is caused by the pressure side of the blade. The similar results were obtained for the unsteady pressure phase distribution (see Fig. 19).

3. Conclusions

1. The comparison of calculated and experimental results for the 1st and 4th Standard Configurations has shown the good quantitative and qualitative agreement for both integral performances (aerodamping coefficient) and local performances (unsteady pressure amplitude and phase distribution).

2. It has shown that the aerodynamic stability (or instability) of oscillating blade row is dependent on the phase shift of the aerodynamic load with respect to the blade motion. The phase shift angle in turn depends on IBPA value.

3. The influence of IBPA on stability (or instability) of the blade row is the distinctive exception of cascade flutter in comparison to the wing flutter.
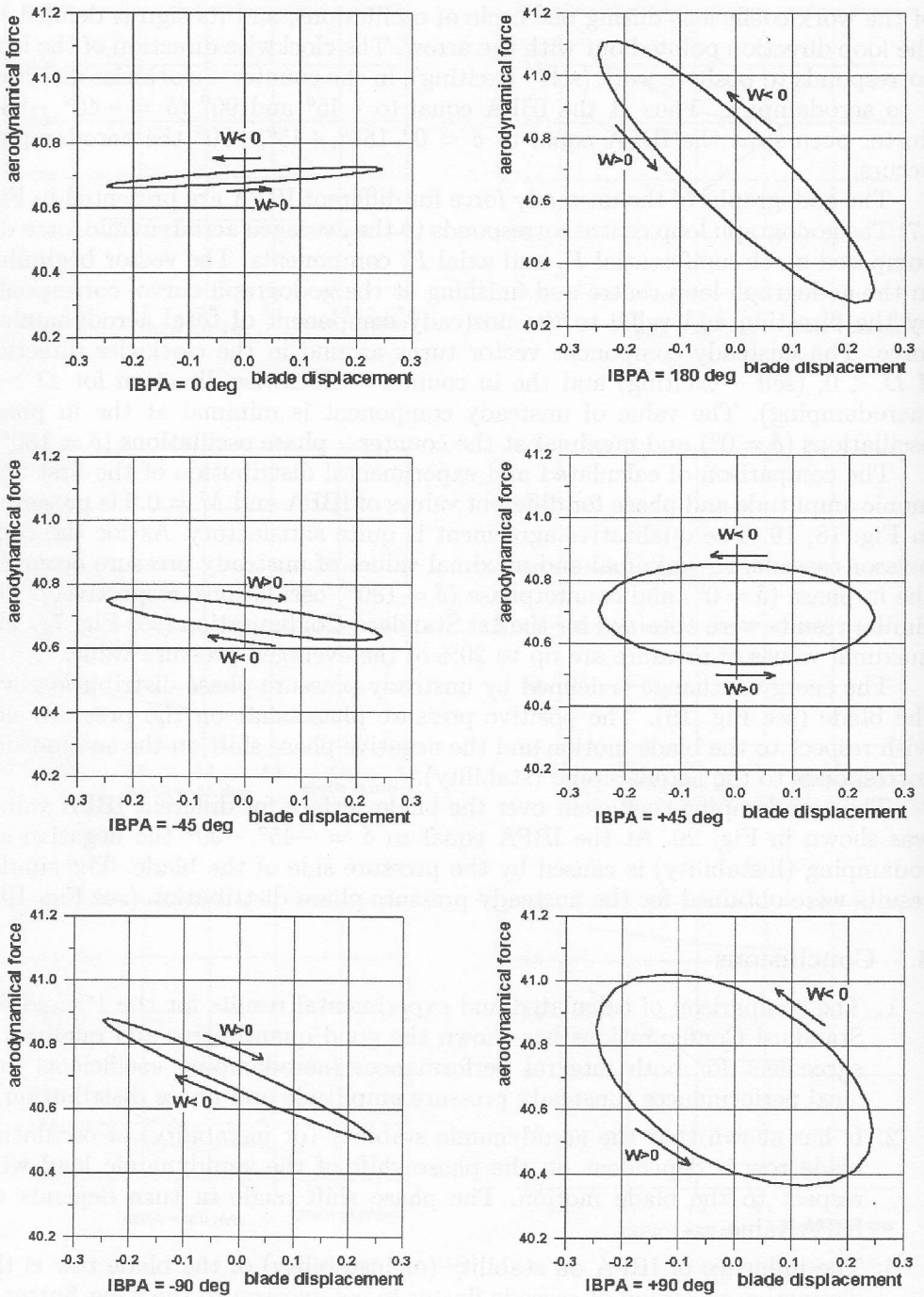
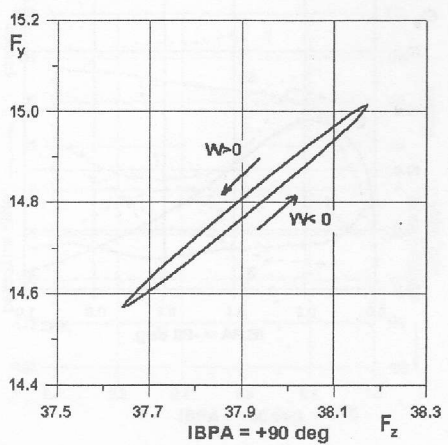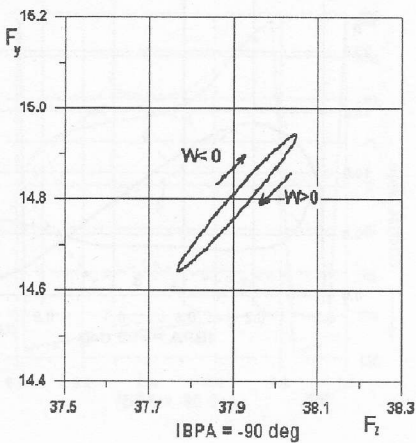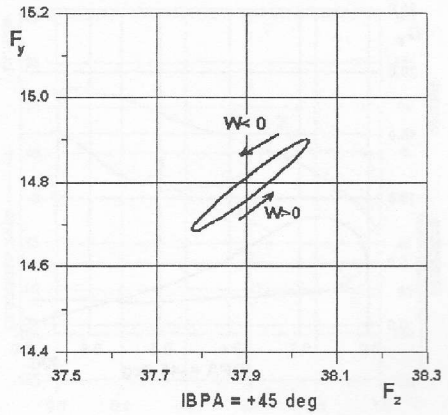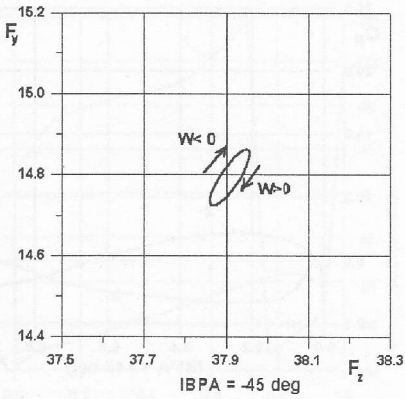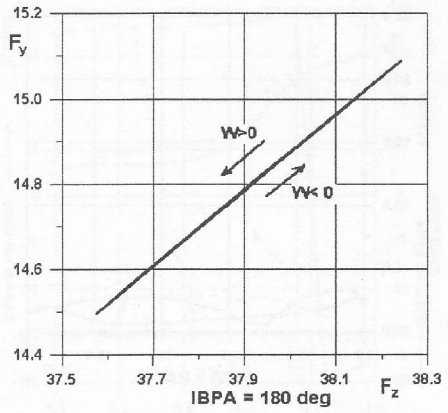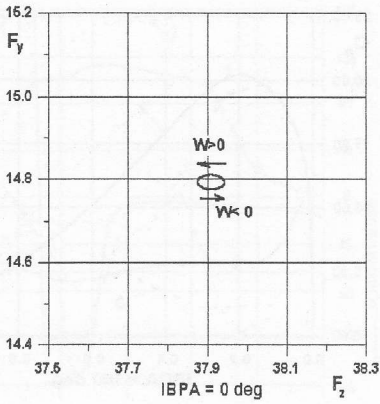Fig. 16. Aerodynamic force in dependence of the blade motion (hysteresis loop).
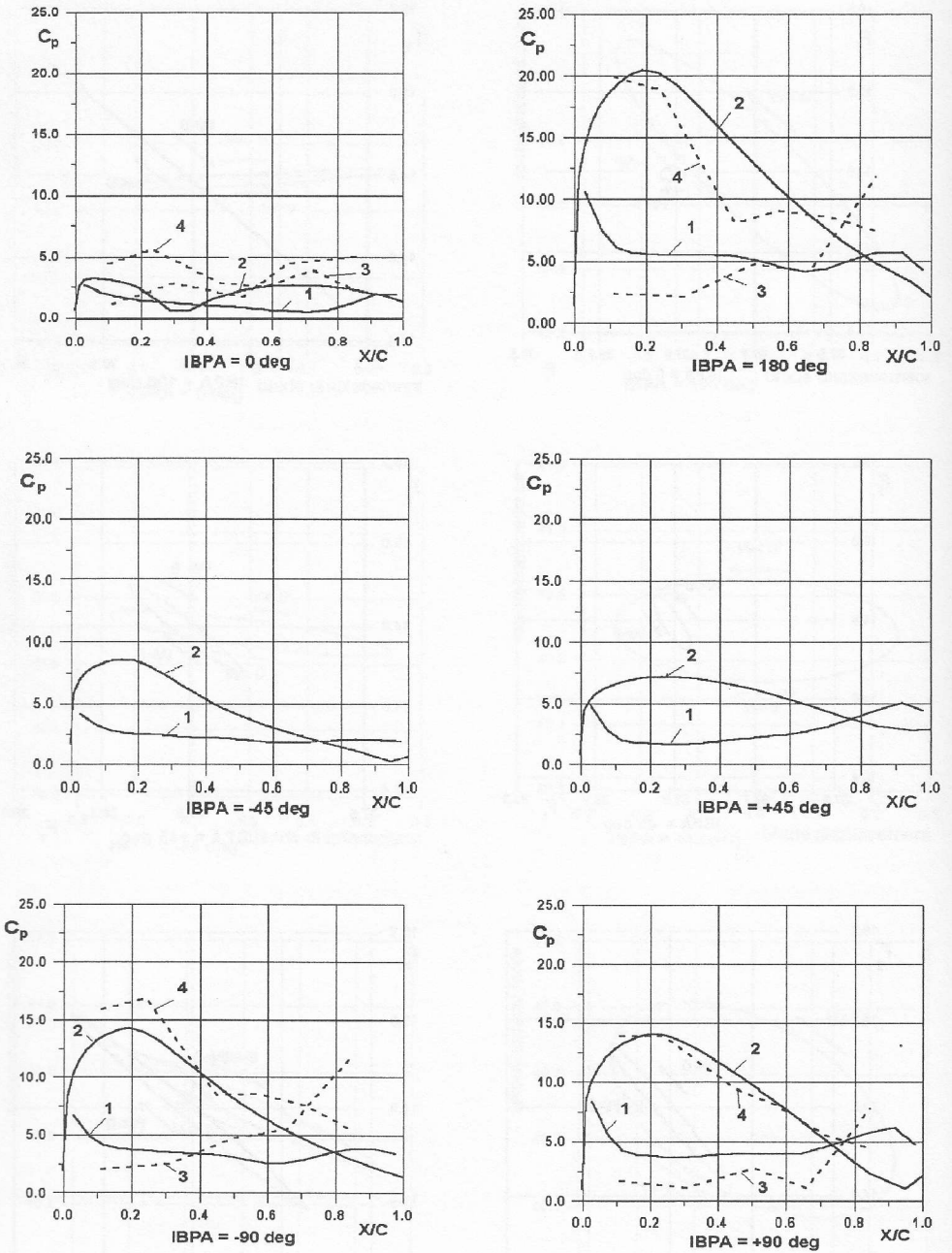
Fig. 17. Aerodynamic force godograph.

Fig. 18. The first harmonic unsteady pressure amplitude distribution over the blade. Theory: 1 – pressure side; 2 – suction side. Experiment: 3 – pressure side; 4 – suction side.
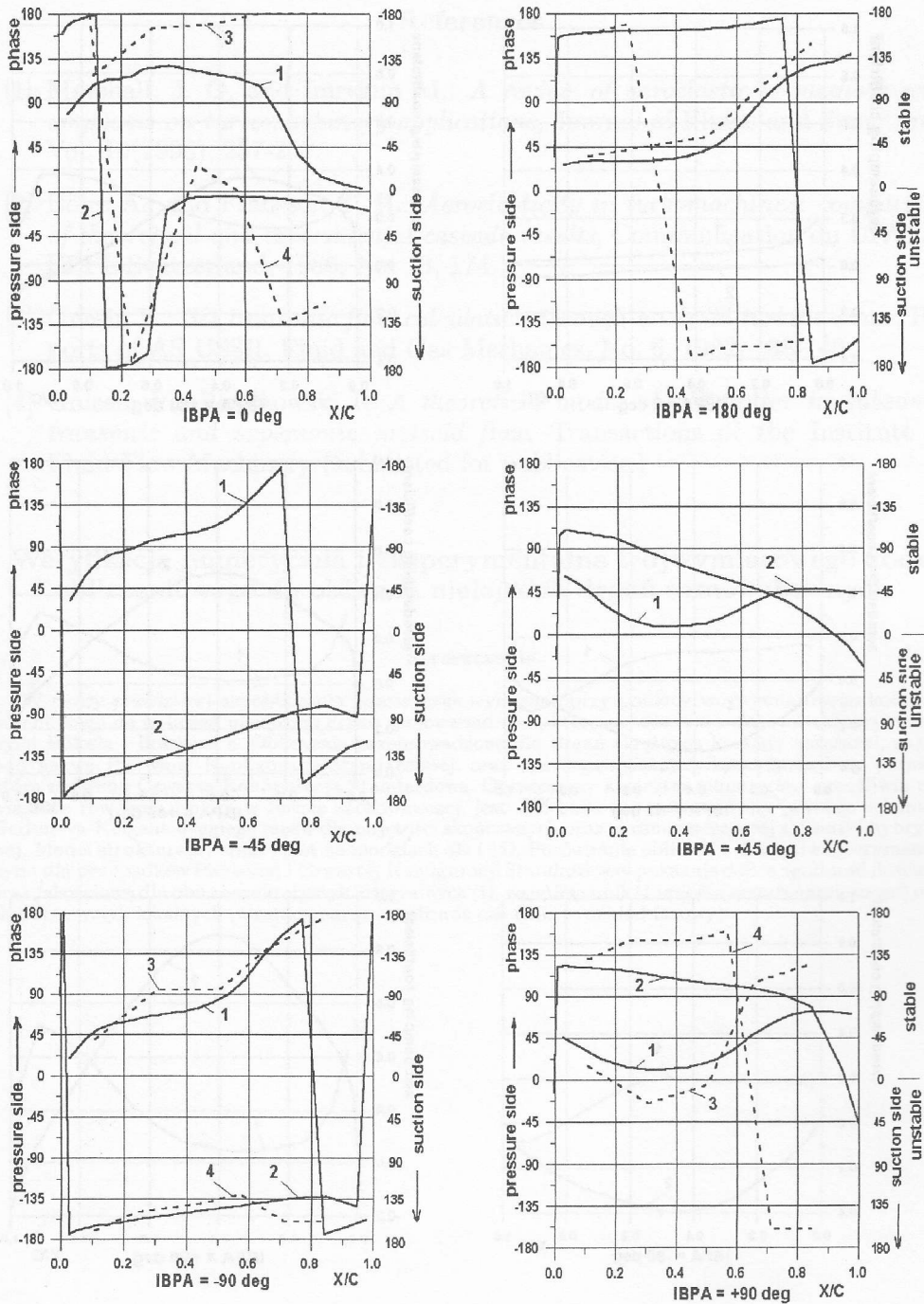
Fig. 19. The first harmonic unsteady pressure phase distribution over the blade. Theory: 1 -- pressure side; 2 – suction side. Experiment: 3 – pressure side; 4 – suction side.
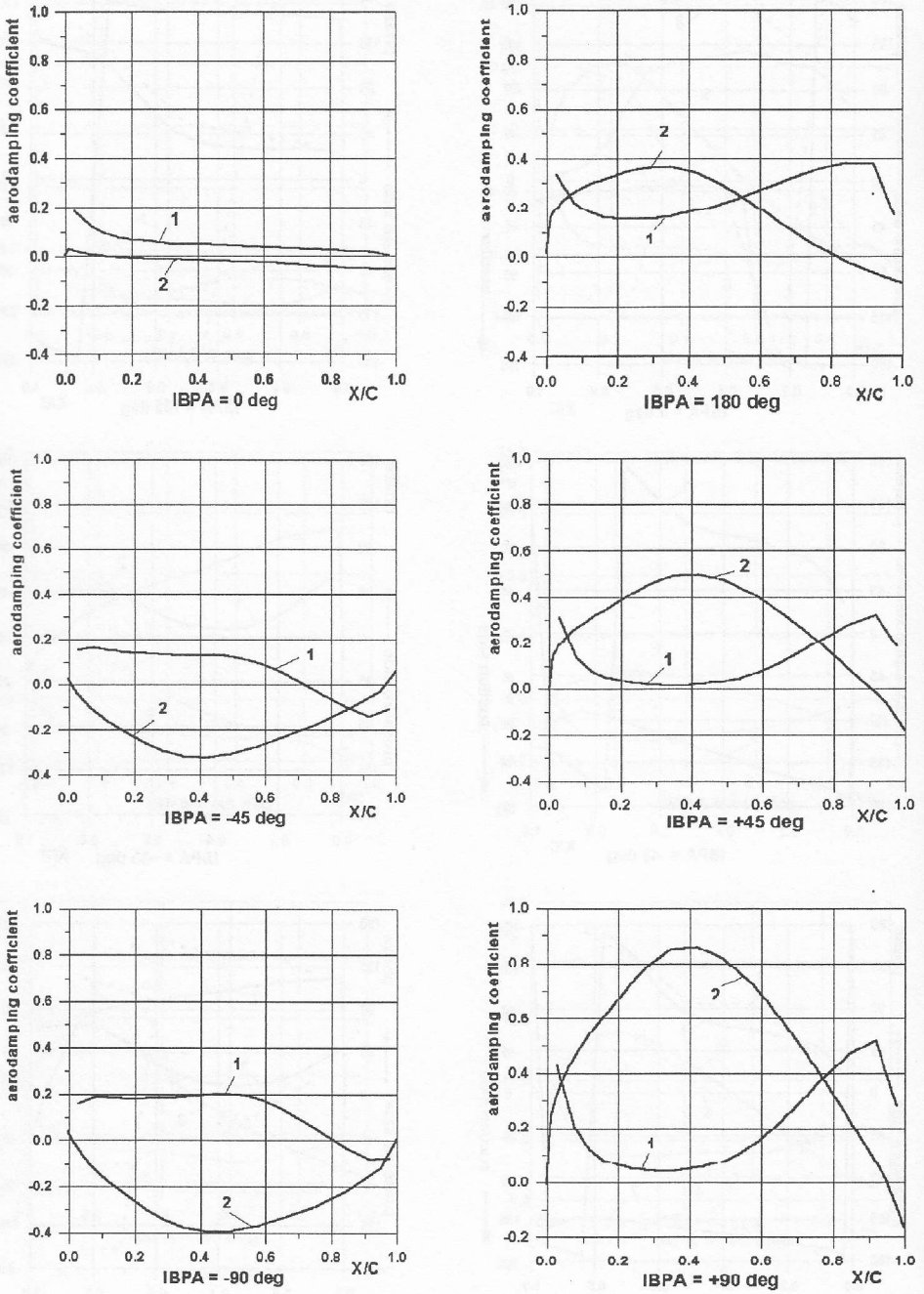
Fig. 20. Aerodamping coefficient versus the blade chord 1 – suction side; 2 – pressure side.

References

[1] Marshall, J. G. and Imregun M.: *A review of aeroelasticity methods with emphasis on turbomachinery applications*, Journal of Fluids and Structures, Vol. 10(1996), 237-257.

[2] Bölcs A., and Fransson T. H.: *Aeroelasticity in turbomachines: comparison of theoretical and experimental cascade results*, Communication du LTAT. – EPFL Switzerland, 1986, No. 13, 174.

[3] Gnesin V.: *3D transonic flow calculation through an axial turbine stage*, Reports of AS USSR, Fluid and Gas Mechanics, No. 6, 1982, 138-146.

[4] Gniesin V., Rządkowski R.:*A theoretical model of 3D flutter in subsonic, transonic and supersonic inviscid flow*, Transactions of the Institute of Fluid-Flow Machinery (submitted for publication)

Weryfikacja numeryczna i eksperymentalna trójwymiarowego kodu obliczeniowego do obliczeń nielepkich drgań samowzbudnych

Streszczenie

W pracy przedstawiono obliczenia numeryczne wykonane przy pomocy trójwymiarowego kodu obliczeniowego do obliczeń nielepkich drgań samowzbudnych, które porównano z danymi eksperymentalnymi Bölcs'a i Fransson'a. Obliczenia przeprowadzono dla drgań skrętnych kaskady sprężarki, znanej pod nazwą Pierwszej Konfiguracji Standardowej, oraz dla drgań giętnych kaskady turbiny parowej, którą nazwano Czwartą Konfiguracją Standardową. Opracowany algorytm numeryczny umożliwia rozwiązanie równania Eulera w formie zachowawczej, jest ono całkowane przy użyciu jawnego schematu Godunova-Kolgana drugiego rzędu dla objętości skończonych oraz przemieszczającej się siatki hybrydowej. Model strukturalny oparty jest na modelach 3D i 1D. Porównanie obliczeń z danymi eksperymentalnymi dla przypadków Pierwszej i Czwartej Konfiguracji Standardowej pokazuje dobrą zgodność ilościową oraz jakościową dla obu charakterystyk integralnych (tj. współczynnik tłumienia aerodynamicznego) oraz charakterystyk lokalnych (niestacjonarna amplituda ciśnienia i rozkład fazowy).